DBTT Reduction Enabled by SiO_2-Bearing Flux in Submerged Arc Welds

The compositional dependence of ductile-brittle transition temperature upon submerged arc welding fluxes for EH36 shipbuilding steel is demonstrated

BY C. HAN, M. ZHONG, H. ZHU, P. ZUO, AND C. WANG

Abstract

The ductile-brittle transition temperature (DBTT) plays a critical role in determining the integrity of welded structures under common low-temperature service conditions. Fluxes are proven effective agents that significantly alter weld compositions and resulting microstructures. In this study, we systematically investigated the impact of programmed SiO_2-containing fluxes upon EH36 shipbuilding steel welds via multi-scale microstructural characterization, instrumented Charpy impact testing, and fractographic analysis. We found that incremental SiO_2 addition from 5 to 40 mass-% drastically enhanced the volume fraction of acicular ferrite from 0.386 to 0.747. As the SiO_2 content increased, the DBTT decreased significantly from −58°C to −97°C but slightly rose to −85°C. Fractographic and secondary-crack analyses indicated that cracks preferentially propagated along grain boundary ferrite and ferrite side plates, whereas crack paths through acicular ferrite were more tortuous. We demonstrated that enhanced toughness is primarily governed by two complementary mechanisms: (1) microstructural refinement through enhanced acicular ferrite fraction, impeding microcrack propagation; (2) minimized presence of large inclusions within coarse ferrite grains, mitigating the risk of premature cleavage fracture initiation. Such findings highlight that superior low-temperature toughness necessitates balanced grain refinement and precise control over inclusions. Overall, we showcased a cost-effective strategy geared toward achieving optimized weld microstructures and mechanical performances merely by adjusting welding fluxes, which could also shed light on the development of high-performance welding consumables for alternative low-temperature structural steel.

Keywords

- Submerged Arc Welding
- Weld Metal
- Ductile-Brittle Transition Temperature
- Impact Toughness
- Inclusion

Introduction

Structural steel must operate above corresponding ductile-brittle transition temperatures (DBTTs) to maintain sufficient toughness and avoid brittle fracture (Refs. 1, 2). Cold-weather structures—from pipelines, ships, offshore platforms operating in cold oceans to icebreakers cruising in polar regions—warrant effective approaches that can lower the DBTT to withstand extreme conditions (Refs. 1, 3). These stringent demands apply not only to the base metals but also to derivative welded joints (Refs. 3, 4).

The ductile-brittle transition arises from a competition between plastic deformation and brittle fracture at the tips of cracks or flaws within the steel (Ref. 1). The process can be modulated through strategies such as grain refinement, which suppresses brittle fractures, or controlled delamination techniques, which enhance plastic deformation (Refs. 1, 2). However, welding is typically the final step for practical manufacturing processes, rendering it impossible to obtain a delamination structure through thermomechanical treatment. Therefore, for low-carbon low-alloy steels, the prevailing strategy to enhance weld metal (WM) tough-

https://doi.org/10.29391/2025.104.031

ness involves refining the effective grain size to achieve a microstructure predominantly composed of acicular ferrite (AF) (Refs. 5, 6). AF forms intragranularly on selected non-metallic inclusions, creating fine, interlocking plates that partition parent austenite (γ) grains, impede cleavage crack propagation, and enhance toughness (Refs. 6, 7). Beyond adjustments to welding procedure parameters, efforts to promote AF formation in WMs typically follow two paths. One involves adjusting WM composition using different filler metals (Ref. 8) or metal powder additions (Ref. 9). The other of great interest is to manipulate flux compositions in submerged arc welding (SAW) (Refs. 10–13).

During SAW, fluxes—commonly composed of CaF_2 and/or oxides such as SiO_2, MnO, and TiO_2—decompose at high temperatures, driving possible chemical reactions at the slag-metal-gas interfaces (Ref. 14). These reactions influence alloying element transfer and alter WM chemistry conveniently, thereby altering inclusion features, salient microstructures, and, ultimately, mechanical properties (Refs. 14, 15). For instance, Bang et al. (Ref. 13) examined the influence of flux composition and basicity on elemental transfer behaviors and the resultant impact toughness of WMs. Their findings indicated that a flux with high basicity could achieve lower weld O content, contributing to an appreciable improvement in the impact toughness. Dallam et al. (Ref. 10) identified an optimal O content (i.e., inclusion quantity) in WMs using CaF_2-CaO-SiO_2 fluxes for maximizing AF presence, hence promoting toughness. Similarly, Zhang et al. (Ref. 11) and Paniagua-Mercado et al. (Ref. 12) showed that TiO_2 addition into commercial fluxes could all generate sizeable Ti-containing inclusions and drastically enhanced weld toughness due to elevated AF fraction.

While these efforts highlight the importance of flux design, they largely focus on adjusting flux basicity or increasing the fraction of AFs in the microstructure to achieve superior toughness. However, such endeavors often neglect the dual effect of inclusions, which are the critical factor in determining WM toughness. In addition to inducing AF formation, inclusions introduced by fluxes may also be accommodated within brittle microstructural constituents—such as grain boundary ferrite (GBF), ferrite side plate (FSP), and bainite—that form around the parent γ grain boundaries (PAGBs), thereby acting as potential sources of cleavage cracks. (Refs. 16, 17) Brittle cleavage, as a "weakest link" controlled process, may easily lead to catastrophic crack propagation and severely compromise toughness (Refs. 16–19). Consequently, inclusions may serve as double-edged swords: While they facilitate AF nucleation and microstructural refinement, improving toughness, they may also trigger ductile or cleavage fractures (Ref. 20). The challenge, therefore, is to develop flux strategies that simultaneously encourage AF formation and minimize possible detrimental effects enabled by inclusions as potential crack initiation sites.

A promising pathway involves controlling both the columnar γ grain (CG) size and inclusion population. Previous studies have indicated that a microstructure characterized by relatively large CGs and a controlled number of inclusions facilitates AF formation while suppressing GBF, FSP, and bainite (Refs. 6, 20, 21). Achieving such a balance—tailoring CG development and inclusion characteristics—holds the key to lowering the DBTT and enhancing the low-temperature toughness of low-carbon low-alloy steel WMs.

Recently, we have demonstrated that the SiO_2 content in fluxes could notably affect both CG size (Ref. 22) and inclusion characteristics (Ref. 23) in the WMs of EH36 shipbuilding steel, which will inevitably alter their weld microstructure. These findings inspired us to explore the toughening strategies of low-carbon low-alloy steel submerged-arc welds using SiO_2-bearing fluxes. In the present study, SAW trials were conducted on EH36 shipbuilding steels utilizing binary CaF_2-SiO_2 fluxes, emphasizing the influence of SiO_2 content on microstructural evolution and impact toughness. Multiscale microstructural characterization, instrumented Charpy impact tests, and fractographic analyses were performed to clarify the underlying toughening mechanisms. These findings may provide valuable guidance for designing welding fluxes to precisely control WM properties in challenging low-temperature service environments.

Experimental

Materials Preparation

Fused binary CaF_2-SiO_2 fluxes were prepared with programmed SiO_2 contents (5, 20, and 40 mass-%). Fluxes were prepared from reagent-grade chemicals of CaF_2 (> 98.5 mass-%) and SiO_2 (> 99.7 mass-%) (all from Sinopharm Chemical Reagent Co. Ltd). For each flux composition, 3.0 kg of powder was accurately blended based on the desired mass ratio. To achieve uniformity, the blended materials were pre-melted at 1550°C in a graphite crucible for 1 h. The pre-melted fluxes were then quenched in cold water, followed by drying at 700°C for 2 h to eliminate moisture. After drying, the fluxes were crushed and sieved to a particle size range of 8 to 40 mesh for use in SAW.

EH36 shipbuilding steel, a typical low-carbon low-alloy steel, was selected as the base plate and welded in the rolling direction using SAW with a heat input of 60 kJ/cm. To investigate the impact of the solidification sequence and the resulting CG size on microstructural evolution, two types of EH36 steel with different carbon contents were used. These were classified as low carbon (BM-L) and high carbon (BM-H) within the composition range specified by ASTM A131, *Standard Specification for Structural Steel for Ships*. The weld samples produced using BM-L were labeled as S5, S20, and S40 based on their nominal SiO_2 mass percentages. The weld sample obtained by welding BM-H with CaF_2-40 SiO_2 was labeled S40H. The designations of the welds, along with the corresponding base materials and flux compositions, are summarized in Table 1.

SAW Processing

High heat-input bead-on-plate submerged arc welding experiments were carried out on flat EH36 shipbuilding steel plates (24 mm thick) employing a Lincoln Electric Power Wave® AC/DC 1000® SD welding machine (Lincoln Electric, China). A single-pass, double-wire tandem con-

Table 1 — Designations of the Welds Along with Corresponding Base Materials and Flux Compositions

WMs	Base Materials	Flux Compositions
S5	BM-L	CaF_2-5%SiO_2
S20	BM-L	CaF_2-20%SiO_2
S40	BM-L	CaF_2-40%SiO_2
S40H	BM-H	CaF_2-40%SiO_2

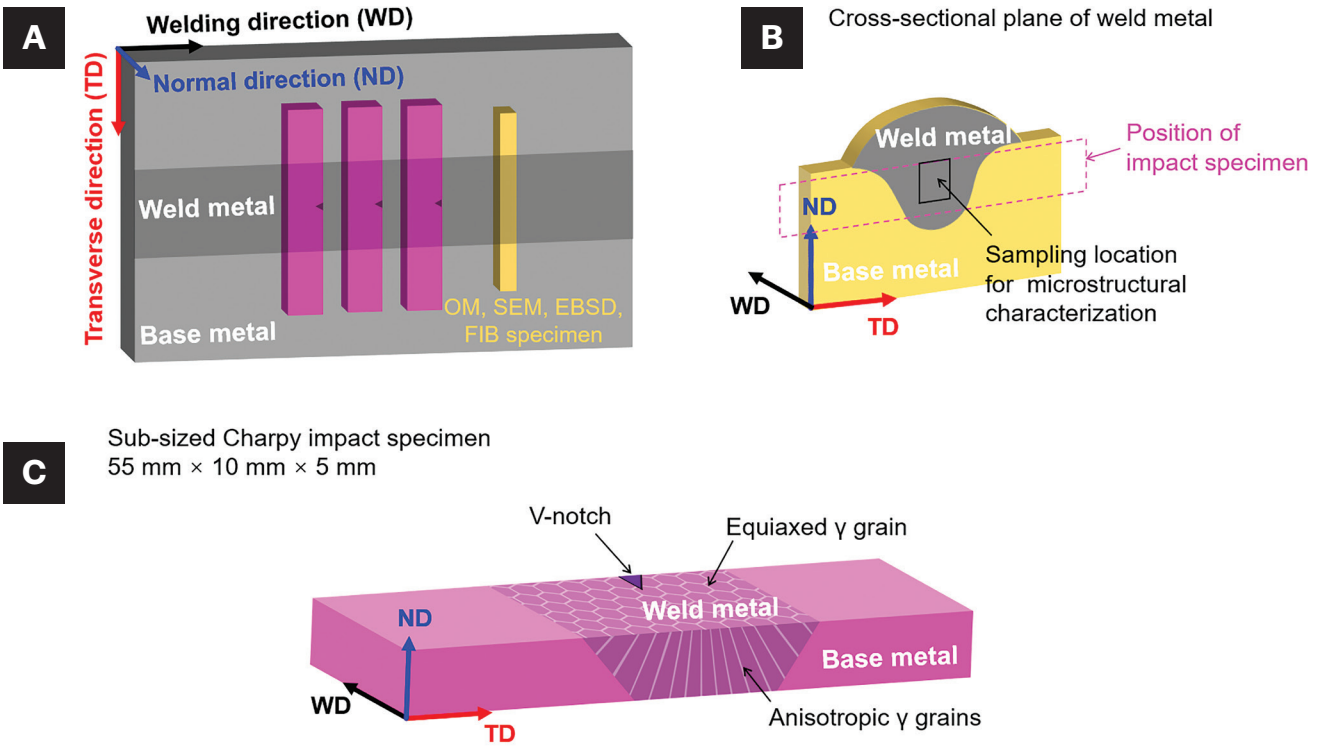

Fig. 1 — Schematic diagrams showing: A — The three-dimensional orientation of the impact specimens relative to the EH36 shipbuilding steel plate, including the specimen used for microstructural analysis; B — cross-sectional plane of WM showing the sampling location for microstructural characterization (black box) and relative position of the impact specimen (pink dashed box); C — the parent γ grain structure in the impact specimens. ND is the normal direction; WD is the welding direction; TD is the transverse direction.

figuration was adopted, embracing welding parameters of DC-850 A/32 V for the leading electrode and AC-625 A/36 V for the trailing electrode. A commercial 4-mm-diameter electrode wire (CHWS3, Atlantic, China) was utilized. The contact tip-to-workpiece distance was controlled at 25 mm, and the electrical stick-out was approximately 15 mm. The spacing between the front and rear electrodes was fixed at 20 mm. Welding was conducted at a constant travel speed of 500 mm/min to achieve a heat input of approximately 60 kJ/cm. To ensure the reliability and comparability of the experimental results, the welding parameters and process conditions were strictly kept identical across all trials. After welding, a weldment with an overall length of about 30 cm was obtained, featuring a uniform weld bead extending approximately 15 cm. For each flux composition, three equivalent weldments were obtained, providing a total of approximately 45 cm of uniform weld bead for subsequent microstructural characterization and mechanical property testing.

Metallic elements in the base metals, electrode wire, and WMs were characterized using inductively coupled plasma optical emission spectrometry (ICP-OES, Optima 8300, Perkin-Elmer). The O and C contents were measured using LECO

Table 2 — Chemical Compositions of Base Metals, Wire, and WMs (mass–%)

Employed Materials	C	Si	Mn	Al	Ni	Cr	Mo	Ti	O
BM-L	0.075	0.195	1.26	0.035	0.362	0.124	0.061	0.016	0.0028
BM-H	0.175	0.260	1.44	0.060	0.010	0.020	0.006	0.010	0.0046
Wire	0.127	0.049	1.65	0.008	0.009	0.030	—	0.010	0.0030
S5	0.081	0.139	1.19	0.006	0.201	0.085	0.035	0.007	0.0169
S20	0.072	0.231	1.05	0.009	0.192	0.091	0.027	0.007	0.0240
S40	0.060	0.327	0.97	0.015	0.211	0.096	0.046	0.007	0.0397
S40H	0.124	0.364	1.07	0.017	0.015	0.096	0.004	0.006	0.0403

analyzers (ONH836 for O and CS230 for C). The resulting chemical compositions are listed in Table 2.

Microstructure Characterization and Quantification

Each sample for microstructural analysis and impact testing was extracted from the WM under stable welding conditions (Fig. 1A). For microstructural characterization, samples were extracted from the central region of the WM cross-section, with a 1.0 mm offset from the steel plate surface. In this configuration, the characterized region was located internally relative to the ND-TD (normal direction-transverse direction) plane of the impact specimen, as schematically illustrated in Fig. 1B. Microstructural observation was conducted on the WM cross-sectional plane using a field-emission scanning electron microscope (FESEM, MIRA3, TESCAN, Czech Republic) at 20.0 kV with a 15 mm working distance. The specimens were mechanically ground with 800, 1200, and 2000 grit silicon carbide papers, mirror polished with a 0.25 μm diamond suspension, and etched in a 4 vol-% nital solution for 5 s. Phase identification was performed via x-ray diffraction (XRD, Rigaku DMAX-RB with Cu Kα radiation).

Electron backscatter diffraction (EBSD) analysis was carried out on the rolling, normal, and transverse planes using an EBSD system (Nordlys Nano, Oxford Instruments, United Kingdom). The EBSD specimens were electrolytically etched in a solution of 5 vol-% perchloric acid and 95 vol-% ethanol at 20 V for 90 s. EBSD measurements were performed at 20 kV with a 17 mm working distance, using step sizes of 0.8 and 0.5 μm depending on the required magnification. Ferrite grain sizes, expressed as equivalent circle diameters, were measured using at least 10 EBSD maps (normal direction) at 1000× magnification.

For metallographic analysis, weld samples were examined on the cross-sectional plane corresponding to the WM region enclosed by the pink dashed box, using an optical microscope (OM, GX51, Olympus, Japan), as shown in Fig. 1B. The volume fractions of the microstructural constituents in the WM were quantitatively determined using the point-counting method embedded within the ImageJ software with a 500-point grid applied to at least 36 fields. The parent γ grain size was measured as the "width" of the columnar grains—taken normal to their major axis on the transverse section of the WM—using the linear intercept method as recommended for anisotropic structures in ASTM E112, *Standard Test Methods for Determining Average Grain Size*, with detailed measurement procedures available elsewhere (Ref. 22).

Inclusion Examination

Inclusion analysis was performed on the central area of mirror-polished specimens from all WMs (Fig. 1B). At 5000× magnification, an FESEM operating at 20.0 kV with a 15 mm working distance was used to measure inclusion size and quantity. For each WM, at least 100 fields of view were analyzed, covering a total area of approximately 0.230 mm^2. Additionally, a lamella sample was prepared using focused ion beam scanning electron microscopy (FIB-SEM, Thermo Fisher Scientific Scios 2) to enable selected area electron diffraction patterns (SADPs) of inclusions through transmission electron microscopy (TEM, Tecnai F20). During sample preparation, a target inclusion was initially identified from the polished sample (5 mm × 10 mm × 2 mm) etched with 4 vol-% nital solution. It was then protected with a Pt layer to prevent ion milling damage. Subsequently, a lamella measuring approximately 12 μm × 5 μm × 0.7 μm crossing the selected inclusion was extracted and further thinned to below 80 nm by ion milling.

Charpy Impact Toughness Test

Charpy impact toughness tests were performed using a Charpy impact tester (PIT302D, Shenzhen Wance Testing Machine Co. Ltd., China) with a 300 J capacity and a CDW-196

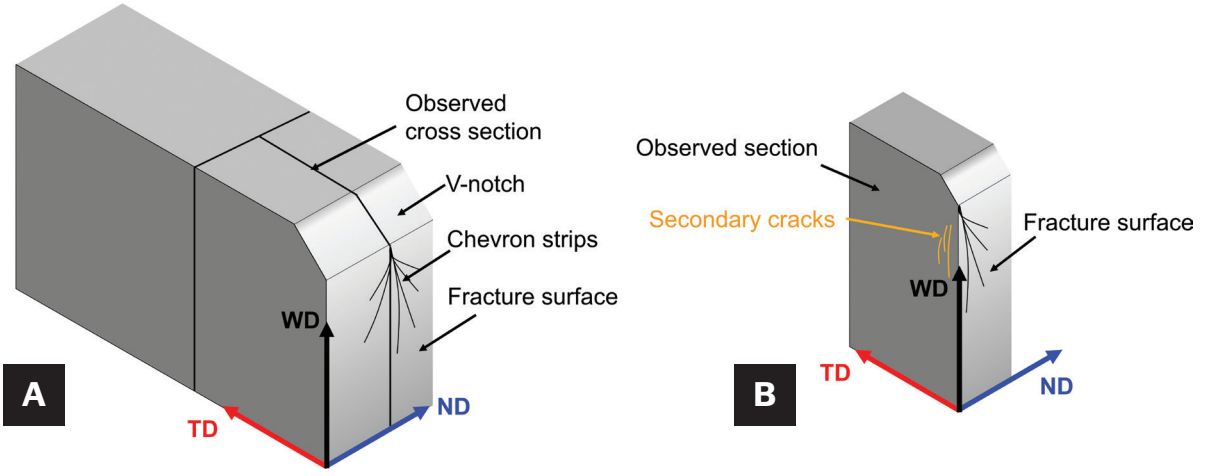

Fig. 2 — Metallographic sections for observing the cracks retained in a fractured specimen: A — Cutting direction; B — metallographic section revealing retained cracks pointed to by the orange arrow.

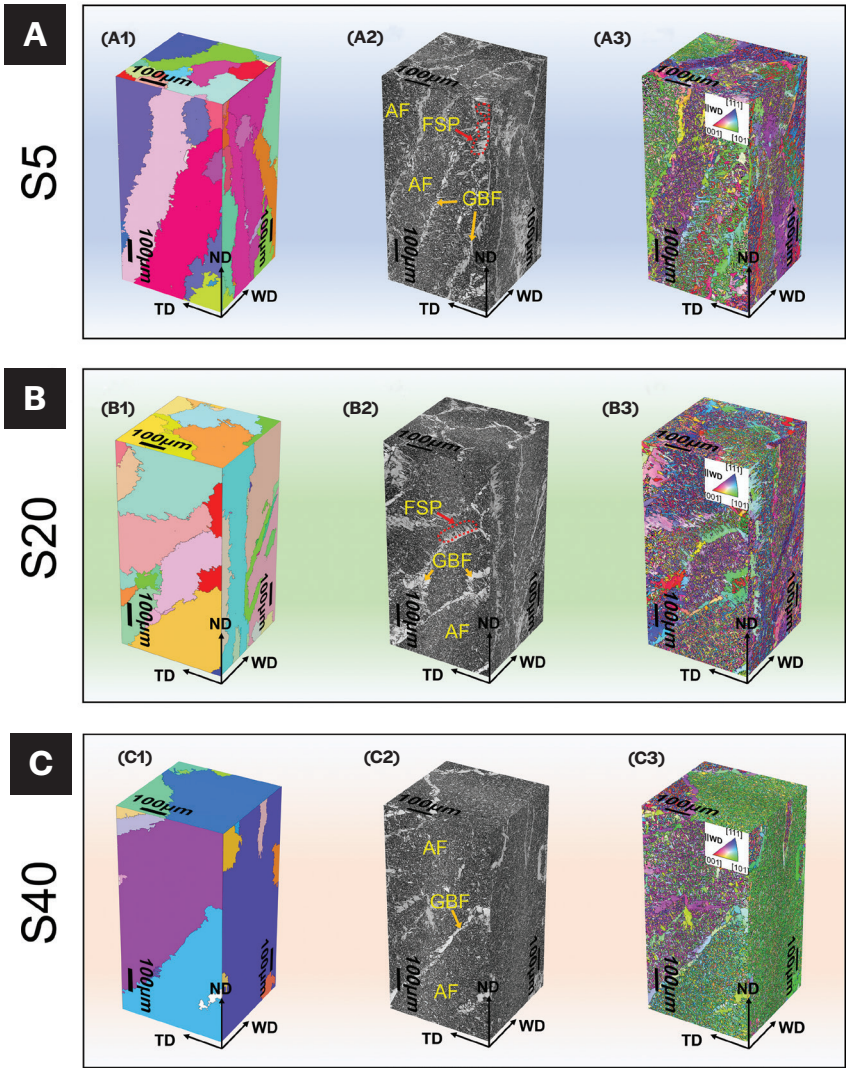

Fig. 3 — Microstructural evolution of submerged arc WMs: A — S5; B — S20; C — S40. A1, B1, C1 — Three-dimensional (3D) stereographic mean crystallographic orientation maps of the reconstructed parent γ with columnar shape, obtained through the MTEX Toolbox (Ref. 25); A2, B2, C2 — EBSD band contrast maps; A3, B3, C3 — EBSD inverse pole figure maps.

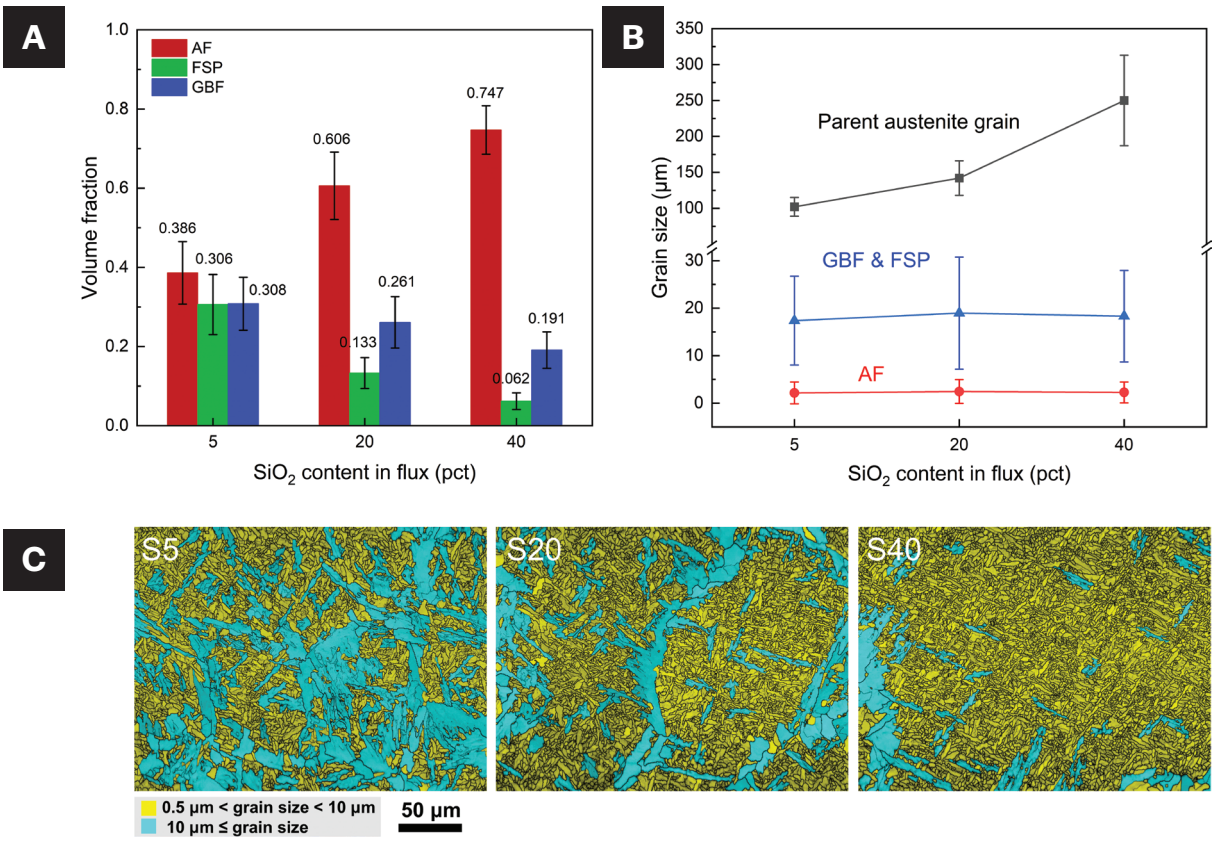

Fig. 4 — Quantitative results of WM microstructure: A — Variation of microstructural constituents in the weld as a function of SiO_2 content in the flux; B — variation of parent austenite grain and ferrite grain sizes with SiO_2 content; C — EBSD grain size map.

low-temperature chamber, in accordance with ISO 9016:2022, *Destructive tests on welds in metallic materials — Impact tests — Test specimen location, notch orientation and examination*. Additionally, instrumented Charpy impact tests were conducted at −60°C using an instrumented impact tester (ZBC2452-DE, MTS, United States) following ISO 14556:2023, *Metallic materials — Charpy V-notch pendulum impact test — Instrumented test method.* The penetration depth of the welds varied from 6.61 to 11.82 mm, depending on the flux composition, as also reported in our previous study (Ref. 22). To ensure that fracture occurred entirely within the WM, subsized V-notched impact specimens (5 × 10 × 55 mm^3, ASTM E23, *Standard Test Methods for Notched Bar Impact Testing of Metallic Materials*) were used for impact testing. At least 30 impact specimens were extracted from the welded components perpendicular to the welding direction (WD) (see Fig. 1A), with a 1.0 mm offset from the steel plate surface. For each flux composition, Charpy V-notch impact specimens were tested at multiple temperatures to construct the ductile-to-brittle transition curve, with a minimum of three replicate specimens tested per temperature point to ensure statistical reliability. As shown in Fig. 1C, a 2 mm-deep V-notch with an angle of 45 deg, oriented parallel to the WD, was machined at the center of each specimen. Impact tests were carried out over a temperature range from liquid nitrogen temperature (LNT, −196°C) to room temperature (RT, 20°C), with cooling by liquid nitrogen. Temperature was monitored using an attached K-type thermocouple.

After impact testing, secondary cracks beneath the fracture surface of Charpy impact specimens tested at LNT were observed at 5000× magnification using an FESEM operating at 20.0 kV with a 15 mm working distance. As shown in Fig. 2, the cross-section was prepared perpendicular to the fracture surface, where secondary cracks were observed at a depth of approximately 250 μm below the V-notch root (Ref. 24).

Results

Weld Microstructures

Figures 3 (A1, B1, C1) show the reconstructed 3D stereographic parent γ grains. It can be seen that these grains exhibited columnar shapes. Furthermore, they unanimously demonstrated anisotropic morphologies on both the WD and transverse direction (TD) planes while possessing an approximately equiaxed structure on the ND plane. As the SiO_2 content increased from 5 to 40 mass-%, the CG size grew, expanding from approximately 150 μm to over 250 μm (Ref. 22). Figures 3 (A2, B2, C2) present corresponding EBSD band contrast maps, from which it can be found that the weld microstructure was mainly composed of GBF, FSP, and AF. From the XRD patterns (Figs. A-1 A–C), the diffraction peaks of the body-centered

cubic (BCC) phases exhibited high intensities, whereas the face-centered cubic (FCC)-related peaks were negligible. In agreement with the XRD results, EBSD phase maps (Figs. A-1 D–F) indicate that the weld microstructure predominantly consisted of BCC phase. In contrast, the proportion of the FCC-related retained γ structure was < 0.1%. Inverse pole figure maps (Figs. 3A3, B3 and C3) show that coarse GBFs and FSPs were distributed along PAGBs, while fine AF laths, exhibiting different spatial orientations, were located within parent γ grains. Figures A-1 (G–I) clearly illustrate that PAGBs were decorated with GBFs measuring 10 to 30 μm in width, while FSPs, ranging from 20 to 60 μm in length, extended from PAGBs into parent γ grains. In contrast, densely packed AF plates developed intragranularly, partitioning parent γ grains with high-angle grain boundaries (misorientation angle $\theta \geq 15$ deg). An increase in SiO_2 content led to substantial coarsening of parent γ grains, which appreciably decreased the proportion of PAGBs per unit volume and, consequently, that of GBFs. Additionally, the formation of FSPs was suppressed by the higher quantities of inclusions, which will be discussed later.

Figure 4 presents detailed quantifications of the microstructures in the submerged arc WMs with varying SiO_2 additions. As the SiO_2 content increased, the volume fraction of AFs rose from approximately 0.386 to 0.747, while those of FSPs and GBFs decreased from 0.306 to 0.062 and from 0.308 to 0.191, respectively (Fig. 4A). The mean size of the parent γ grains increased from approximately 102 μm to 250 μm as the SiO_2 content increased from 5 to 40 mass-%. However, the size of the ferrite grains remained unchanged, approximately

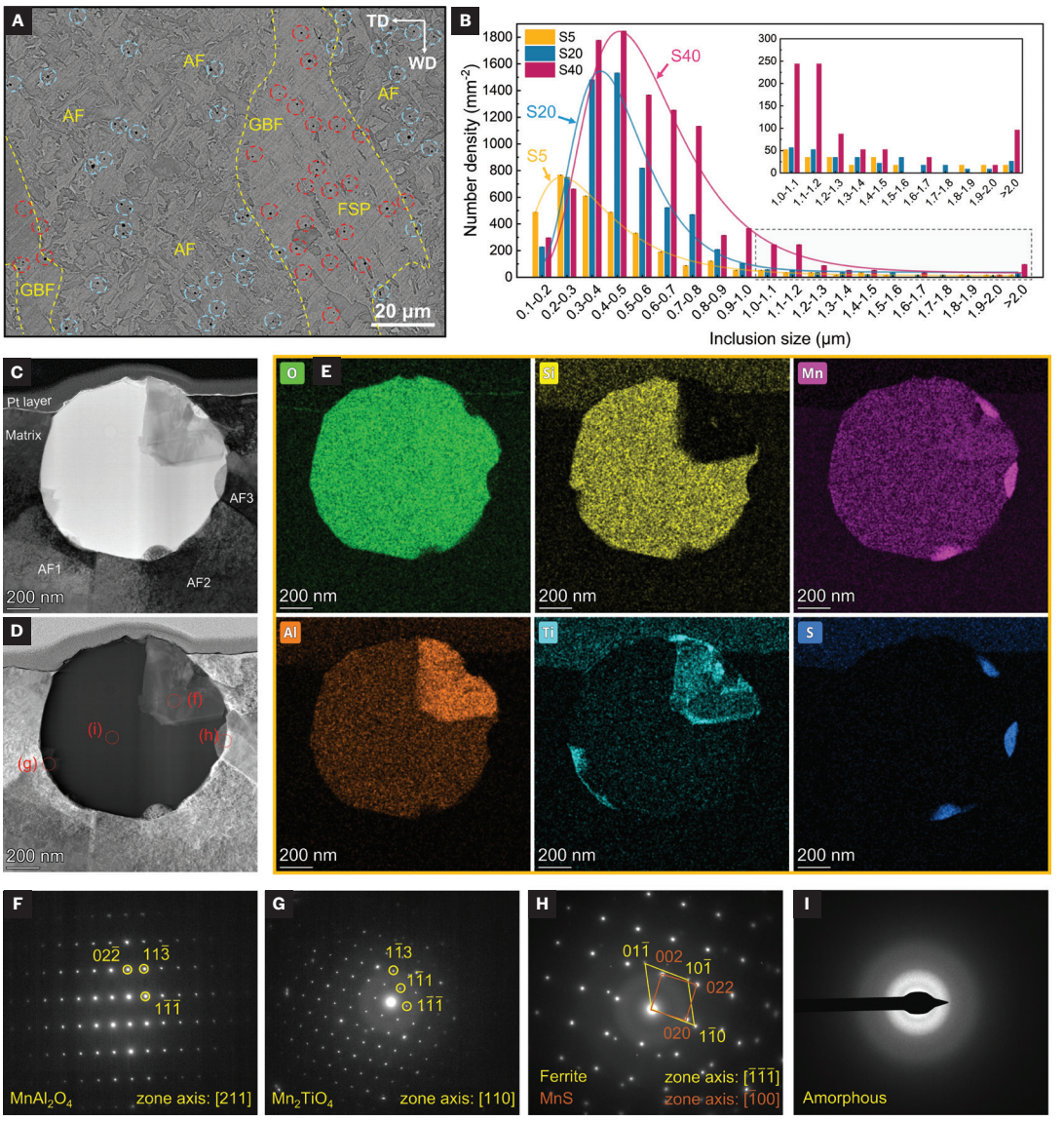

Fig. 5 — Inclusion characteristics in submerged arc WMs: A — SEM BSE image of the S40 microstructure on the ND plane showing inclusions dispersed within GBF and FSP (red dashed circles) and AF (blue dashed circles); B — variations of number density and inclusion size distribution as a function of SiO_2 content. The inset shows the size distribution of inclusions larger than 1.0 μm; C — TEM image (bright field) of a typical inclusion encompassed by AFs; D — TEM image (dark field); E — EDS elemental maps; F–I — selected area electron diffraction patterns (SADPs) circled in (D).

2.30 µm for AFs and around 18.22 µm for GBFs and FSPs (Fig. 4B), while the FSPs typically formed a single grain together with adjacent GBFs.

Quantitative EBSD analysis revealed that with increasing SiO_2 content, the average grain size decreased from 2.696 ± 3.891 µm (S5) to 2.674 ± 3.177 µm (S20) and further to 2.367 ± 2.433 µm (S40). Correspondingly, the coefficient of variation dropped from 1.443 to 1.188 and, finally, to 1.028. These trends indicated that the microstructure became progressively finer and more uniform as the SiO_2 content increased, which could be attributed to the rising proportion of AF in the WM. Due to the substantial size difference between AF and coarse GBF and FSP, the approximately equivalent volume fractions of these constituents in S5 led to a highly heterogeneous grain size distribution. In contrast, AF became increasingly dominant in samples S20 and S40, thus decreasing grain size dispersion. Additionally, since the grain sizes of individual microstructural constituents remain unaffected by flux composition, the observed microstructural refinement primarily resulted from an increased proportion of AF rather than changes in ferrite grain sizes.

These observations are further illustrated in the EBSD grain size maps shown in Fig. 4C. Grains larger than 10 µm, shown in blue, were mainly GBF and FSP, whereas grains smaller than 10 µm, displayed in yellow, corresponded predominantly to AF. As the SiO_2 content increased, the yellow regions gradually dominated, indicating a finer and more uniform microstructure.

Inclusion Characteristics

Figure 5 illustrates inclusion characteristics in the WMs. Inclusions were widely and randomly distributed throughout the weld microstructure (Fig. 5A). Some inclusions were embedded within coarse GBF or FSP regions (red dashed circles). In contrast, others were dispersed inside the parent γ grains (blue dashed circles), where they may have served as nucleation sites for AF plates. Figure 5B shows histograms of the inclusion size distributions and corresponding log-normal fitting curves for S5, S20, and S40. As the SiO_2 content increased, the inclusion number density rose significantly—from 3377 mm^{-2} in S5 to 6424 mm^{-2} in S20 and 9836 mm^{-2} in S40. In S5, the inclusion diameter predominantly peaked at 0.2–0.3 µm; in S20, the peak shifted to 0.3–0.4 µm; and in S40, it shifted further to 0.4–0.5 µm. The number of inclusions larger than 1.0 µm in S40 (827 mm^{-2}) was significantly higher than in S5 (243 mm^{-2}) and S20 (313 mm^{-2}). Figures 5C and D show TEM bright field and dark field images of the typical inclusion inducing AF plate formation in the WM, respectively. Corresponding EDS elemental maps (Fig. 5E) illustrate that the inclusion core was mainly composed of Si-Mn-Al-O phase, with minor amounts of (Al, Ti)-bearing phases and MnS precipitates present on the surface. Figures 5F–I are selected area diffraction patterns (SADPs) of positions marked in the dark-field image of Fig. 5D. The SADPs of these four distinct phases indicate that the inclusion consisted of an amorphous Si-Mn-Al-O phase (Fig. 5I), accompanied by crystalline $MnAl_2O_4$ (Fig. 5F) and Mn_2TiO_4 (Fig. 5G) phases as well as MnS precipitates (Fig. 5H). It is widely acknowledged that complex inclusions, particularly oxide inclusions combined with MnS precipitates, are highly effective in facilitating the nucleation of AF microstructures in steels (Refs. 26, 27).

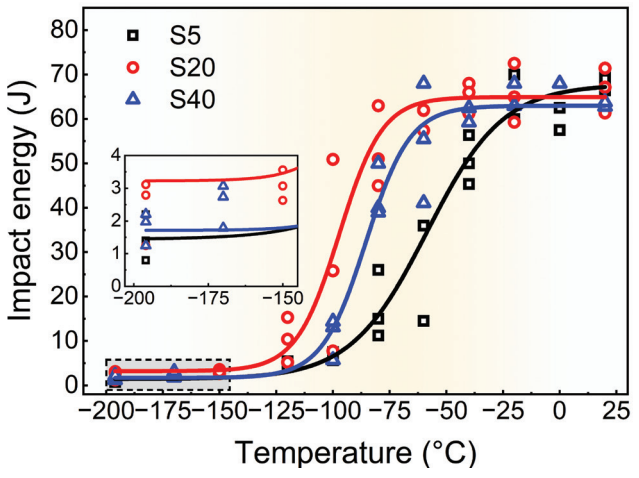

Fig. 6 — Variation in Charpy V-notch impact energy as a function of testing temperature for welds: S5, S20, and S40.

Impact Toughness

Figure 6 shows the results of Charpy 45 deg V-notch tests conducted over a wide temperature range from LNT to RT to assess the relationship between impact toughness and SiO_2 content in the flux. These impact testing results were fitted with the Boltzmann function (Equation 1), which was proven to be the best-fitting equation among several regression models (Refs. 28–30):

$$E = \frac{A_1 - A_2}{1 + exp\left[\frac{T - T_t}{\theta_1}\right]} + A_2 \quad (1)$$

where E is the Charpy impact energy (J), A_1 and A_2 are the lower shelf energy and upper shelf energy, respectively (J), T is the temperature (°C), T_t is the DBTT at the 50% transition threshold between the lower and upper shelf energies, and θ_1 is the fitting parameter. Charpy V-notch impact energy (vE) of S5 dropped sharply as the temperature decreased from RT to −120°C, resulting in a DBTT of −58°C. In contrast, S20 maintained relatively high vE values (approximately 65 J) from RT to −80°C, significantly lowering DBTT to −97°C. At −80°C, S20 achieved an average vE of 58 J—more than three times higher than that of S5. However, it should be noted that the vE of S20 sharply declined into the lower-shelf region when temperatures further decreased to −120°C. Surprisingly, despite having the highest AF content, S40 showed lower vE values across the entire tested temperature range compared to S20, accompanied by an increased DBTT of −85°C.

Discussion

Weld Microstructure Evolution

The decomposition of SiO_2 in the flux occurs at the plasma/slag interface under the influence of the welding arc (Refs.

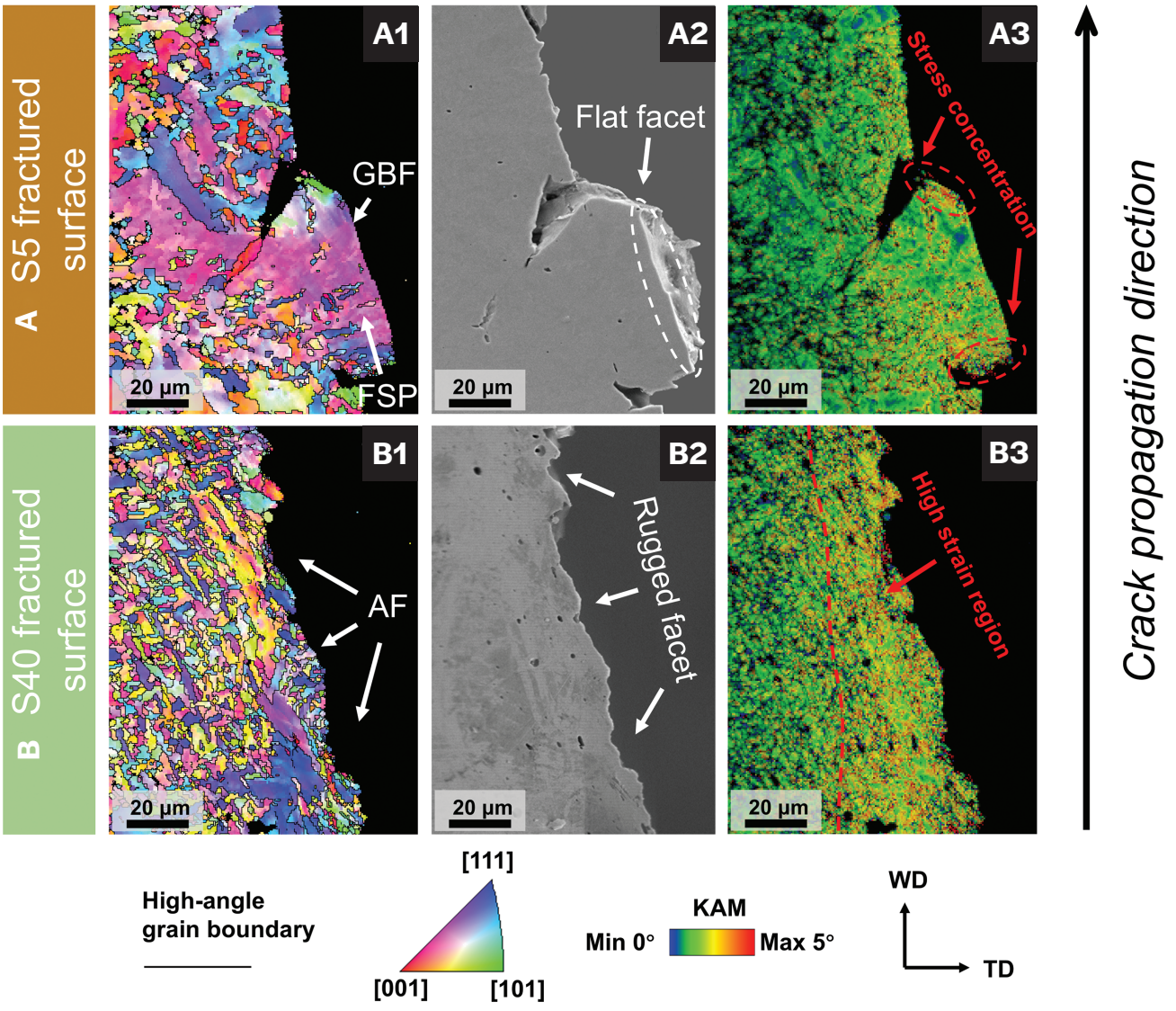

Fig. 7 — A1 and B1 — EBSD IPF-ND maps; A2 and B2 — SEM fractographic images; A3 and B3 — KAM distribution maps taken from the ND plane of the weld (A) S5 and (B) S40 specimens fractured at –60°C.

14, 31). The effect of SiO_2 on element transfer behaviors has been well documented, as its addition enables Si and O transfer from the flux to the WM, which promotes decarburization and Mn loss from the WMs (see Appendix B). These elemental transfers, as reflected in the changes in Table 2, lead to the following effects:

1. The weld solidification path is shifted from peritectic to primary δ solidification, primarily due to decarburization of the WM (Ref. 22).

2. Inclusion quantity is significantly elevated within the WM due to remarkable O gain (Ref. 23).

During weld microstructural formation, the CG structure typically dominates, with its size being controlled by the solidification process. Finer-grain structures are generally associated with the peritectic process, whereas coarser γ grains tend to form after primary δ solidification (Refs. 22, 32). Thus, incorporating SiO_2 into the flux coarsens the CG size, as demonstrated by the reconstructed parent γ images in Figs. 3A1, B1, and C1 and supported by our recent findings (Ref. 22).

During γ → α phase transformation upon further cooling, PAGBs serve as favorable nucleation sites for α-ferrite (Refs. 6, 20). However, particles such as complex oxides (Ref. 33) can also act as active nucleation sites for ferrite plates, competing with grain boundaries under certain conditions (Refs. 6, 20). Increasing the SiO_2 content coarsens parent γ grains, thereby reducing the total surface area of PAGBs per unit volume and decreasing the likelihood of GBF and FSP nucleating at PAGBs (Ref. 20). In contrast, a higher number density of complex inclusions distributed throughout the microstructure enhances intragranular nucleation of ferrite, which promotes the formation of AF at the expense of FSP (Refs. 6, 20).

To verify these observations, we designed an additional WM, S40H (Table 1). Compared to S40, the extra C provided

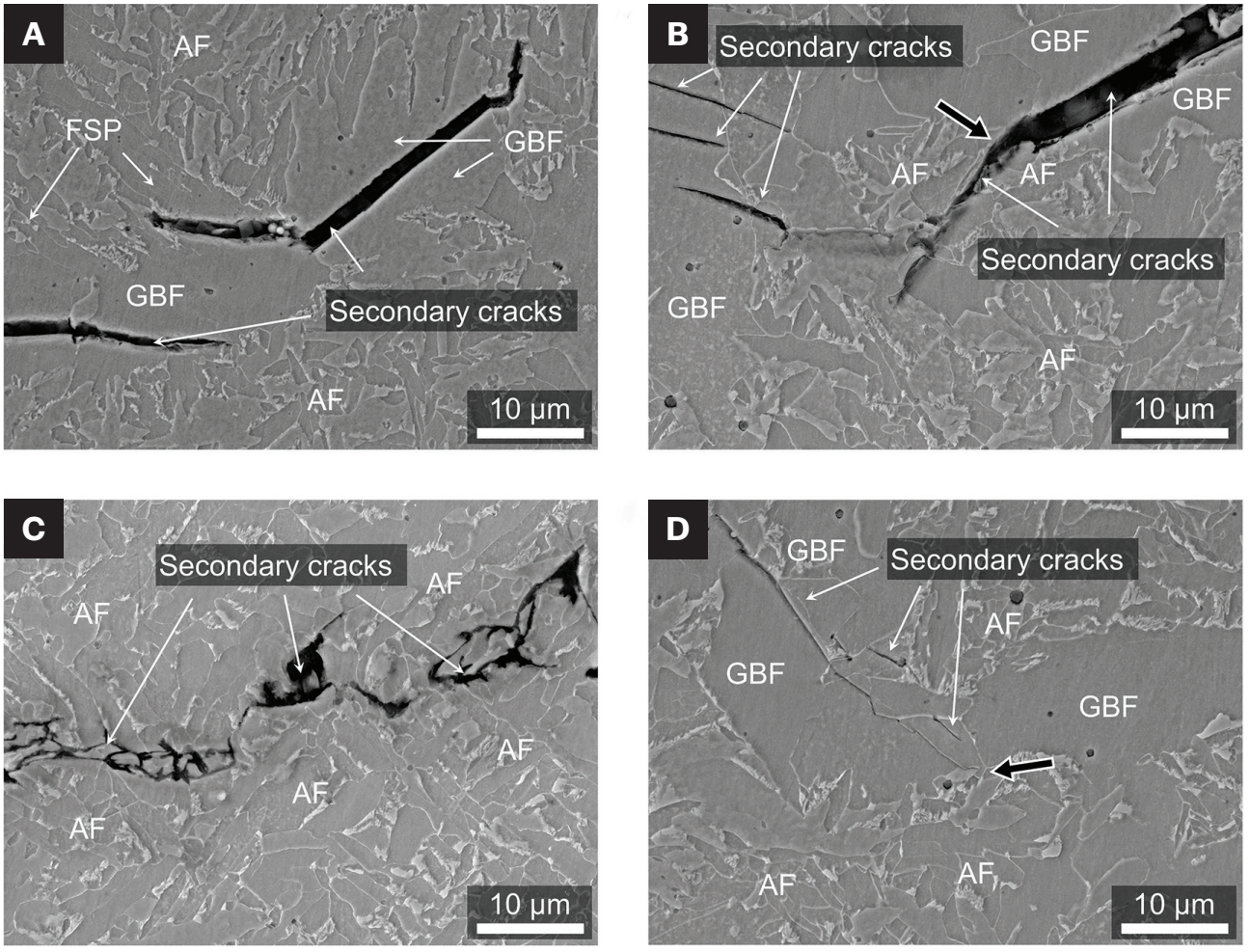

Fig. 8 — SEM micrographs showing typical secondary cracks beneath the fracture surface of Charpy impact specimens tested at LNT in A, B — S5; and C, D — S40. The black arrows in B and D highlight the deflected and arrested crack positions due to AFs.

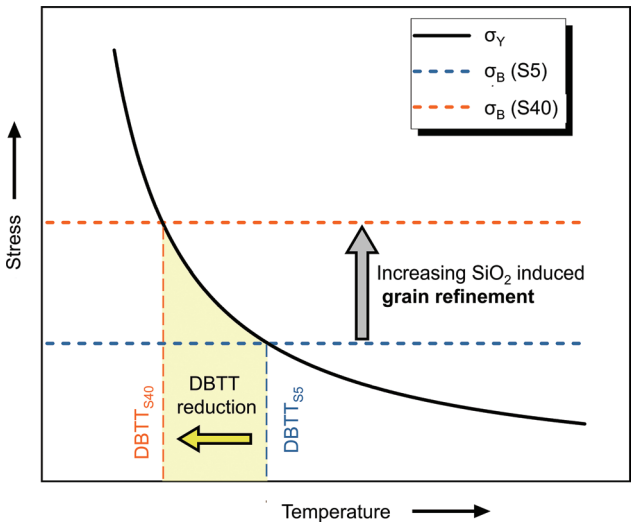

Fig. 9 — Schematic Yoffee diagram illustrating the reduction in DBTT due to increased SiO_2 content in the flux.

by BM-H allowed S40H to maintain a peritectic composition, resulting in the formation of fine parent γ grains (Ref. 22). Although S40H has an O content similar to S40 (and, thus, a comparable number of inclusions), its finer CGs (84 ± 8 μm) offer a substantially larger surface area of PAGBs per unit volume, resulting in more-abundant nucleation sites for GBF and FSP formation (Fig. A-2). The detailed quantification results of S40H are shown in Table A-1. Consequently, SiO_2 in the flux exerts two synergistic effects on microstructure refinement: (1) by shifting the solidification path toward a non-peritectic sequence via decarburization, coarse CGs were produced, and (2) by increasing the number of intragranular inclusions, intragranular AF nucleation was enhanced. Together, these effects increased AF proportion while decreasing volume fractions of coarse GBF and FSP.

Grain Refinement-Induced Toughening

In the present study, S20 and S40—with AF as the dominant microstructure—exhibited improved toughness and possessed lower DBTTs compared to S5, the microstructure

of which was primarily composed of coarse GBFs and FSPs. To further elucidate underlying toughening mechanisms, crack path analysis was performed on two representative samples: S5 (dominated by GBFs and FSPs) and S40 (with a maximum AF content), as shown in Fig. 7. Figures 7A1 and B1 reveal that in S5, local cracks propagated along GBF and FSP in the observed region, whereas cracks in S40 primarily propagated through AF structures. Corresponding to the crack path along coarse GBF and FSP in S5, typically flat, brittle fracture facets were observed (Fig. 7A2). In contrast, cracks traversing AF in S40 exhibited a severely tortuous propagation path, suggesting that crack propagation encountered higher resistance, thereby contributing to a more ductile fracture mode (Fig. 7B2) (Ref. 34).

Additionally, the KAM map (Fig. 7B3) reveals that S40, characterized by dominant AFs, exhibited a high-strain region near the fracture surface, indicating enhanced absorption of impact energy through plastic deformation. In contrast, regions dominated by coarse GBFs and FSPs, as depicted in Fig. 7A3, showed limited capability to impede trans-granular crack propagation. This limitation was featured by lower KAM values near flat fracture facets and localized stress concentrations adjacent to these coarse-grained regions.

Observations of secondary crack propagation beneath the fracture surface can reveal the microstructural constituents least resistant to cleavage fracture (Ref. 18). Figure 8 shows the typical secondary cracks micrographs of Charpy impact specimens tested at LNT. The results showed that the cracks preferentially propagated along GBFs and FSPs in a straight line (Fig. 8A); they were either deflected (Fig. 8B), followed a zigzag path through the AF region (Fig. 8C), or were arrested by AF laths (Fig. 8D).

The relationship between the observed crack propagation behavior and toughness can be further understood using the Yoffee diagram, which states that the ductile-brittle transition occurs when the effective yield stress (σ_Y) surpasses the brittle fracture stress (σ_B), resulting in brittleness and reduced toughness in steels (Ref. 1). Grain refinement effectively enhances σ_B by reducing the mean free path for cleavage cracks, forcing them to deviate or arrest at ferrite grain boundaries or other crystallographic discontinuities. Consequently, this promotes ductile fracture at lower temperatures and reduces the DBTT (Refs. 1, 5). As demonstrated in Fig. 9, increasing the SiO_2 content promoted the formation of a fine and dense AF microstructure, elevating σ_B relative to σ_Y. This effectively lowered the DBTT and encouraged a more ductile fracture mode. The toughness enhancement of fine AF microstructures is attributed to their high density of high-angle grain boundaries, which act as barriers to cleavage crack propagation, compelling cracks to adjust their microscopic propagation paths according to local crystallography (Refs. 6, 7).

Interestingly, specimen S20, despite having a lower AF fraction compared to S40, exhibited superior low-temperature toughness and the lowest DBTT. This suggests that additional toughening mechanisms may have been involved, warranting further investigation.

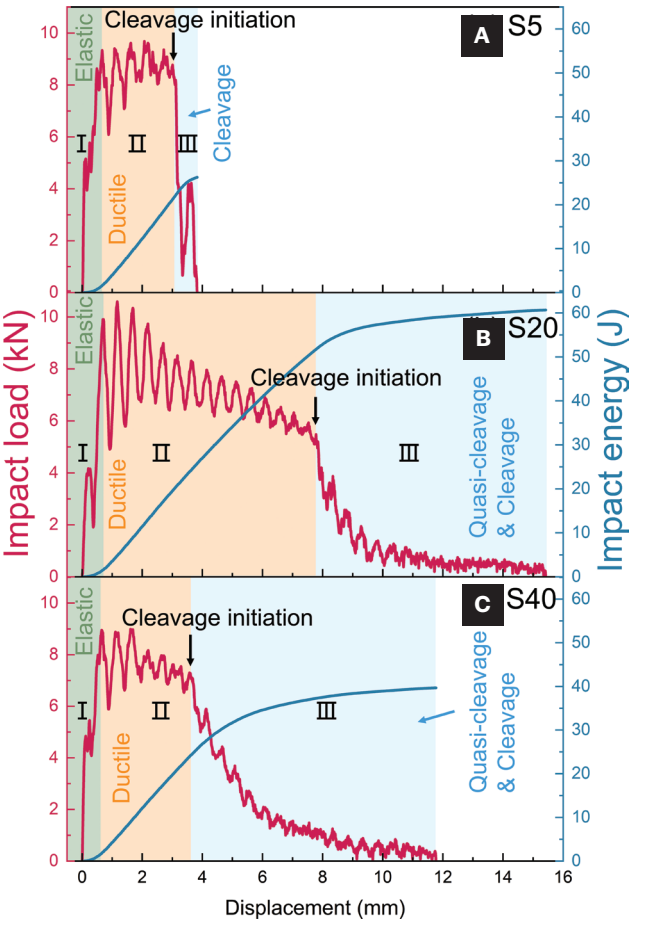

Fig. 10 — Relations between impact load and displacement during instrumented impact tests for: A — S5; B — S20; C — S40 conducted at –60°C.

Effect of Inclusions on DBTT

To further examine the fracture behavior of the weld samples during the ductile-brittle transition, instrumented Charpy impact tests were conducted on S5, S20, and S40 at –60°C. The corresponding impact load-displacement (F-S) curves in Fig. 10 can be largely divided into three regions. In Region I, all specimens exhibited a similar trend, with the impact load (F) increasing linearly with displacement (S), corresponding to elastic deformation. In Region II, F continued to rise until plateauing, followed by a gradual decline, indicating steady-state ductile crack propagation (Ref. 35). Notably, the displacement distance corresponding to Region II of the S20 significantly exceeded that of S5 and S40, suggesting enhanced impact energy absorption. In Region III, F dropped abruptly to zero in S5, preventing further energy absorption. In contrast, S20 and S40 showed a more gradual decrease in F, allowing additional energy absorption.

Figure 10 illustrates that the total impact energy consists of two main components: energy absorbed during steady-state ductile crack propagation (Region II) and energy consumed during cleavage or quasi-cleavage crack propagation after cleavage initiation (Region III). Although S40 followed a similar trend to S20, the extended steady-state ductile region

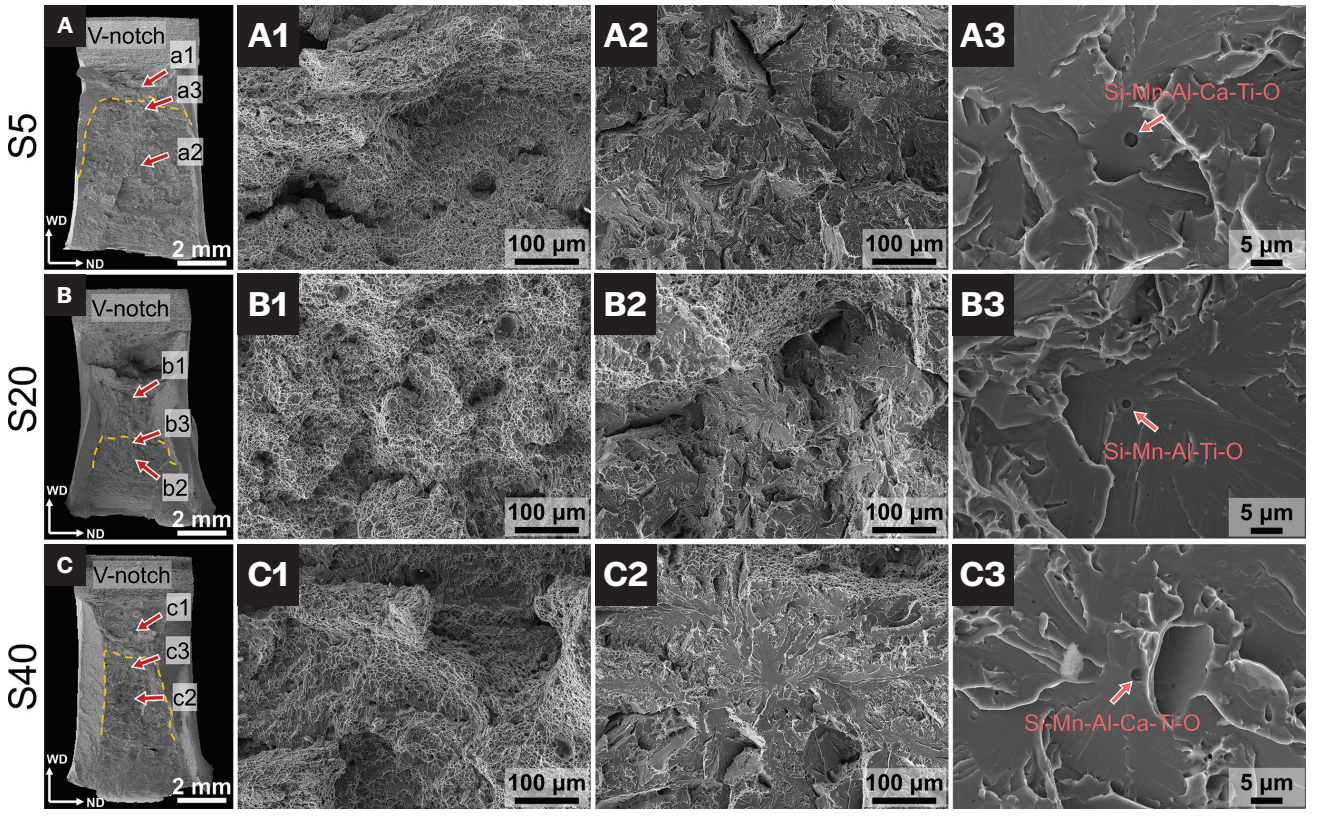

Fig. 11 — Fractographs of the instrumented Charpy impact tested specimens: A — S5; B — S20; C — S40 at −60°C, respectively. The orange dashed lines delineate the fibrous crack regions from the quasi-cleavage/cleavage fracture regions. A1–A3, B1–B3, and C1–C3 are the magnified images of the locations marked in A–C.

Table 3 — Number Density of Inclusions Acting as Potential Crack Initiation Sources in Weld Specimens Determined by SEM-BSE Imaging and Corresponding DBTT

WMs	Number Density of Potential Crack Initiation Sources (mm^{-2})	DBTT (°C)
S5	231	−58
S20	148	−97
S40	158	−85
S40H	292	−21

in S20 delayed cleavage initiation, resulting in higher impact energy than S40. Additionally, the abrupt drop in F to zero in Region III for S5 was most likely incurred by the unique microstructure dominated by coarse GBFs and FSP, which promoted brittle crack propagation with minimal energy absorption once cleavage occurred. In contrast, in S20 and S40, where AF was the dominant component, crack propagation was deflected or hindered by the AF structure even after cleavage initiation, leading to significantly increased energy absorption in Region III.

Fractographic analysis from instrumented Charpy impact tests (Fig. 11) supported these observations. All specimens initially showed fibrous cracks characterized by fine dimple patterns (Figs. 11A1, B1, and C1), which were eventually arrested by regions displaying cleavage or quasi-cleavage (Figs. 11A2, B2, and C2) fracture modes. Crack initiation sites were typically associated with composite inclusions larger than 1 μm (Figs. 11A3, B3, and C3). Notably, S20 displayed a longer fibrous crack extension than S5 and S40, consistent with the results in Fig. 10. Previous studies (Refs. 4, 36) reported a near-linear correlation between vE and fibrous crack length, while Chen et al. (Ref. 18) indicated that in the DBTT region, cleavage fracture limited toughness by halting fibrous crack extension. Thus, preventing premature cleavage initiation is critical for improving weld low-temperature toughness beyond achieving an AF-dominated microstructure.

Previous studies (Refs. 17, 19) have identified three stages in the cleavage fracture process: (1) microcrack initiation within inclusions; (2) crack propagation across the inclusion/matrix interface into adjacent matrix grains; and (3) crack propagation through grain boundaries into surrounding grains. The critical stress for cleavage fracture is influenced by inclusion size (d) and effective surface energy (γ), as described by the Griffith Equation 2 (Ref. 37):

$$\sigma = \left(\frac{\pi E \gamma}{(1-\nu^2)d}\right)^{1/2} \quad (2)$$

where E is Young's module and ν is Poisson's ratio. This relationship indicates that larger inclusions decrease the critical stress required for cleavage fracture, rendering them more prone to serve as crack initiation sites. In this study, typical cleavage crack sources were composite inclusions larger than 1 µm in size, which were consistent with findings from Tweed and Knott on C-Mn steel welds (Ref. 16). They also suggested that initial plastic deformation, occurring at low overall strains before fracture and localized within GBF regions, promoted the fracture of inclusions larger than 1 µm embedded within the GBF, thereby creating potential initiation sites for cleavage cracks.

Based on the above discussion, we assumed that inclusions larger than 1 µm located within GBF or FSP were potential crack initiation sources. The number density of such inclusions was statistically analyzed by using at least 100 SEM-BSE images at 5000× magnification for each weld specimen, and the results are shown in Table 3. The results indicated that the number density of potential crack initiation sources initially decreased and subsequently increased with rising SiO_2 content. This trend was consistent with expectations, as the volume fraction of GBF and FSP decreased progressively with SiO_2 addition, while the overall inclusion quantity rose significantly. This counteracting effect ensures the existence of an optimal SiO_2 addition level within 5 to 40 mass-% that minimizes the number of large-sized inclusions (> 1 µm) located within GBF and FSP regions.

Furthermore, the DBTT of WMs decreased with the reduction in number density of potential crack initiation sources, as demonstrated in Table 3. Specifically, in the case of sample S40H, which exhibited a significantly higher number density of crack initiation sources, the DBTT notably increased to as high as –21°C (a complete temperature dependence of vE for S40H is provided in Fig. A-3). Therefore, it is reasonable to expect that lowering the number density of large-sized inclusions embedded in GBF and FSP may will play a decisive role in mitigating cleavage cracking, thereby enhancing fracture toughness.

These findings indicate that optimizing low-temperature toughness in WMs of low-carbon low-alloy steels through flux design requires a balanced strategy. Simply increasing the AF content by introducing inclusions is insufficient to improve toughness and lower the DBTT; the adverse effects of excessive inclusions on toughness must also be carefully considered. While increasing fine AF content, the number of inclusions should be controlled within a reasonable range to minimize large-sized inclusions in GBF and FSP. Consequently, specific elements, such as boron, may be introduced in flux design to inhibit the formation and growth of coarse GBF and FSP along PAGBs. Available studies have shown that boron segregation at PAGBs can reduce grain boundary energy, thus suppressing the nucleation of GBF and FSP (Refs. 20, 38). Pertinent flux design strategies will be systematically elaborated in future endeavors.

Summary

We have investigated the variation in DBTT contingent upon SiO_2 content using SAW on EH36 shipbuilding steel with CaF_2-SiO_2 fluxes. Specifically, the effects of microstructural evolution and inclusions on DBTT were analyzed, as this may contribute to the optimization of the welding flux design for weld toughening. The key findings are summarized as follows:

1. EH36 shipbuilding steel welds produced with fluxes containing 5-40 mass-% SiO_2 exhibited as-deposited WMs composed of GBF, FSP, and AF. Fractographic analysis after Charpy impact tests revealed that GBF and FSP were the weakest constituents, promoting flat, brittle fracture paths. In contrast, cracks propagated in a zigzag manner through AF, indicating greater plastic deformation and a more ductile fracture mode.

2. Increasing the SiO_2 content raised the AF volume fraction from 0.386 to 0.747 at the expense of GBF and FSP. This can be attributed to the combined effects of coarsening of CGs and the increase in the number of inclusions.

3. Typical composite inclusions observed in WMs consisted of an amorphous Si-Mn-Al-O phase accompanied by crystalline $MnAl_2O_4$ and Mn_2TiO_4 phases, along with MnS precipitates. These composite inclusions had two opposing effects on toughness: they facilitated the nucleation of AF, which refined the microstructure and, thus, improved toughness; however, they may have also acted as potential initiation sites for cleavage cracks, hindering fibrous crack propagation and, consequently, reducing low-temperature toughness.

4. As the SiO_2 content increased, the DBTT decreased significantly from –58°C to –97°C but slightly rose to –85°C. Optimal impact toughness, achieved with CaF_2-20 mass-% SiO_2 flux, resulted from a balance between AF-induced grain refinement that hindered microcrack propagation and minimized crack initiation sites within coarse grains (GBF and FSP), reducing the risk of premature cleavage.

Acknowledgments

The authors sincerely thank the financial support from National Natural Science Foundation of China (Grant Nos. W2411047, 52474351, U24A2046, 52350610266), and Major Project of Liaoning Province Innovation Consortium (Grant No. 2023JH1/11200012).

Disclosure Statement

No potential conflict of interest was reported by the author(s).

References

1. Morris, J.W. 2008. Stronger, tougher steels. *Science* 320(5879): 1022–1023. DOI: 10.1126/science.1158994

2. Kimura, Y., Inoue, T., Yin, F., and Tsuzaki, K. 2008. Inverse temperature dependence of toughness in an ultrafine grain-structure steel. *Science* 320(5879): 1057–1060. DOI: 10.1126/science.1156084

3. Ohkita, S., and Horii, Y. 1995. Recent development in controlling the microstructure and properties of low alloy steel weld metals. *ISIJ International* 35(10): 1170–1182. DOI: 10.2355/isijinternational.35.1170

4. Mao, G., Cao, R., Cayron, C., Logé, R., Guo, X., Jiang, Y., and Chen, J. 2018. Microstructural evolution and mechanical property development with nickel addition in low-carbon weld butt joints. *Journal of Materials Processing Technology* 262: 638–649. DOI: 10.1016/j.jmatprotec.2018.07.009

5. Morris Jr, J.W., Lee, C.S., and Guo, Z. 2003. The nature and consequences of coherent transformations in steel. *ISIJ International* 43(3): 410–419. DOI: 10.2355/isijinternational.43.410

6. Díaz-Fuentes, M., Iza-Mendia, A., and Gutiérrez, I. 2003. Analysis of different acicular ferrite microstructures in low-carbon steels by electron backscattered diffraction. Study of their toughness behavior. *Metallurgical and Materials Transactions A* 34(11): 2505–2516. DOI: 10.1007/s11661-003-0010-7

7. Cheng, L., and Wu, K.M. 2009. New insights into intragranular ferrite in a low-carbon low-alloy steel. *Acta Materialia* 57(13): 3754–3762. DOI: 10.1016/j.actamat.2009.04.045

8. Venkateswaran, P., Ganesh Sundara Raman, S., and Pathak, S. D. 2005. Short fatigue crack growth behaviour of a ferritic steel weld metal. *Science and Technology of Welding and Joining* 10(1): 95–102. DOI: 10.1179/174329305X29500

9. Pu, J., Yu, S. F., and Li, Y. Y. 2017. Role of inclusions in flux aided backing submerged arc welding. *Journal of Materials Processing Technology* 240: 145–153. DOI: 10.1016/j.jmatprotec.2016.09.016

10. Dallam, C. B., Liu, S., and Olson, D. L. 1985. Flux composition dependence of microstructure and toughness of submerged arc HSLA weldments. *Welding Journal* 64(5): 140–151.

11. Zhang, J., Leng, J., and Wang, C. 2019. Tuning weld metal mechanical responses via welding flux optimization of TiO_2 content: Application into EH36 shipbuilding steel. *Metallurgical and Materials Transactions B* 50(5): 2083–2087. DOI: 10.1007/s11663-019-01645-6

12. Paniagua-Mercado, A. M., Lopez-Hirata, V. M., Dorantes-Rosales, H. J., Estrada Diaz, P., and Diaz Valdez, E. 2009. Effect of TiO_2-containing fluxes on the mechanical properties and microstructure in submerged-arc weld steels. *Materials Characterization* 60(1): 36–39. DOI: 10.1016/j.matchar.2008.06.003

13. Bang, K. S., Park, C., Jung, H. C., and Lee, J. B. 2009. Effects of flux composition on the element transfer and mechanical properties of weld metal in submerged arc welding. *Metals and Materials International* 15(3): 471–477. DOI: 10.1007/s12540-009-0471-3

14. Wang, C., and Zhang, J. 2021. Fine-tuning weld metal compositions via flux optimization in submerged arc welding: an overview. *Acta Metallurgica Sinica* 57(9): 1126–1140. DOI: 10.11900/0412.1961.2021.00148

15. Chai, C. S. 1980. Slag-metal reactions during flux shielded arc welding. PhD diss., Massachusetts Institute of Technology.

16. Tweed, J. H., and Knott, J. F. 1987. Micromechanisms of failure in C-Mn weld metals. *Acta Metallurgica* 35(7): 1401–1414. DOI: 10.1016/0001-6160(87)90087-3

17. Rodriguez-Ibabe, J. M. 1998. The role of microstructure in toughness behaviour of microalloyed steels. *Materials Science Forum* 284–286: 51–62. DOI: 10.4028/www.scientific.net/msf.284-286.51

18. Chen, J. H., and Cao, R. 2015. *Micromechanism of cleavage fracture of metals*. Boston: Butterworth-Heinemann.

19. Chen, J., and Cao, R. 2017. Micromechanism of cleavage fracture of weld metals. *Acta Metallurgica Sinica* 53(11): 1427–1444. DOI: 10.11900/0412.1961.2017.00145

20. Bhadeshia, H. K. D. H. 2001. *Bainite in Steels: Theory and Practice*. Wakefield, England: Maney Materials Science.

21. Liu, S., and Olson, D. L. 1986. The role of inclusions in controlling HSLA steel weld microstructures. *Welding Journal* 65(6): 139-s to 149-s.

22. Han, C., Zhong, M., Zuo, P., and Wang, C. 2024. SiO_2-bearing fluxes induced evolution of γ columnar grain size. *Welding Journal* 103(10): 362-s to 371-s. DOI: 10.29391/2024.103.031

23. Han, C., Zhong, M., Kaldre, I., Zhao, H., Zhao, P., and Wang, C. 2023. Role of SiO_2 upon weld metal inclusion characteristics in EH36 shipbuilding steels treated by CaF_2-SiO_2 fluxes. *Metallurgical and Materials Transactions B* 54(3): 989–995. DOI: 10.1007/s11663-023-02781-w

24. Mao, G., Cayron, C., Cao, R., Logé, R., and Chen, J. 2018. The relationship between low-temperature toughness and secondary crack in low-carbon bainitic weld metals. *Materials Characterization* 145: 516–526. DOI: 10.1016/j.matchar.2018.09.012

25. Niessen, F., Nyyssönen, T., Gazder, A. A., and Hielscher, R. 2022. Parent grain reconstruction from partially or fully transformed microstructures in MTEX. *Journal of Applied Crystallography* 55: 180–194. DOI: 10.1107/S1600576721011560

26. Sarma, D. S., Karasev, A. V., and Jönsson, P. G. 2009. On the role of non-metallic inclusions in the nucleation of acicular ferrite in steels. *ISIJ International* 49(7): 1063–1074. DOI: 10.2355/isijinternational.49.1063

27. Gamutan, J., Miki, T., and Nagasaka, T. 2020. MnS precipitation behavior in MnO-SiO_2 inclusion in Fe-Mn-Si-O-S alloy system at solid-liquid coexistence temperature. *ISIJ International* 60(8): 1610–1616. DOI: 10.2355/isijinternational.ISIJINT-2019-777

28. Zhao, J. P., Zhang, X. M., and Shen, S. M. 2004. On the method of data processing for ductile-brittle transition temperature. *Petrochemical Equipment* 33(4): 29–32.

29. Wan, Q. M., Wang, R. S., Shu, G. G., Ding, H., Huang, P., Lv, F., and Weng, L. K. 2011. Analysis method of Charpy V-notch impact data before and after electron beam welding reconstitution. *Nuclear Engineering and Design* 241(2): 459–463. DOI: 10.1016/j.nucengdes.2010.11.005

30. Wang, W., Mao, X., Liu, S., Xu, G., and Wang, B. 2018. Microstructure evolution and toughness degeneration of 9Cr martensitic steel after aging at 550°C for 20000 h. *Journal of Materials Science* 53(6): 4574–4581. DOI: 10.1007/s10853-017-1868-x

31. Chai, C. S., and Eagar, T. W. 1982. Slag metal reactions in binary CaF_2-metal oxide welding fluxes. *Welding Journal* 61(7): 229-s to 232-s.

32. Zhang, Z., and Farrar, R. A. 1995. Columnar grain development in C-Mn-Ni low-alloy weld metals and the influence of nickel. *Journal of Materials Science* 30(22): 5581–5588. DOI: 10.1007/BF00356690

33. Zhang, Z., and Farrar, R. A. 1996. Role of non-metallic inclusions in formation of acicular ferrite in low alloy weld metals. *Materials Science and Technology* 12(3): 237–260. DOI: 10.1179/mst.1996.12.3.237

34. Niu, G., Zurob, H. S., Misra, R. D. K., Tang, Q., Zhang, Z., Nguyen, M.-T., Wang, L., Wu, H., and Zou, Y. 2022. Superior fracture toughness in a high-strength austenitic steel with heterogeneous lamellar microstructure. *Acta Materialia* 226: 117642. DOI: 10.1016/j.actamat.2022.117642

35. Sun, J., Wang, H., Xu, B., Jiang, L., Guo, S., Sun, X., Yu, D., Liu, F., and Liu, Y. 2022. Making low-alloyed steel strong and tough by designing a dual-phase layered structure. *Acta Materialia* 227: 117701. DOI: 10.1016/j.actamat.2022.117701

36. Cao, R., Li, J., Liu, D. S., Ma, J. Y., and Chen, J. H. 2015. Micromechanism of decrease of impact toughness in coarse-grain heat-affected zone of HSLA steel with increasing welding heat input. *Metallurgical and Materials Transactions A* 46(7): 2999–3014. DOI: 10.1007/s11661-015-2916-2

37. Bowen, P., Druce, S. G., and Knott, J. F. 1986. Effects of microstructure on cleavage fracture in pressure vessel steel. *Acta Metallurgica* 34(6): 1121–1131. DOI: 10.1016/0001-6160(86)90222-1

38. Oh, D. W., Olson, D. L., and Frost, R. H. 1990. The influence of boron and titanium on low-carbon steel weld metal. *Welding Journal* 69(4): 151-s to 158-s.

39. Zhang, J., Coetsee, T., Dong, H., and Wang, C. 2020. Elucidating the roles of SiO_2 and MnO upon decarburization during submerged arc welding: A thermodynamic study into EH36 shipbuilding steel. *Metallurgical and Materials Transactions B* 51(4): 1805–1812. DOI: 10.1007/s11663-020-01869-x

40. Zhang, J., Coetsee, T., and Wang, C. 2020. Element transfer behaviors of fused CaF_2-SiO_2 fluxes subject to high heat input submerged arc welding. *Metallurgical and Materials Transactions B* 51(1): 16–21. DOI: 10.1007/s11663-019-01753-3.

Appendix A

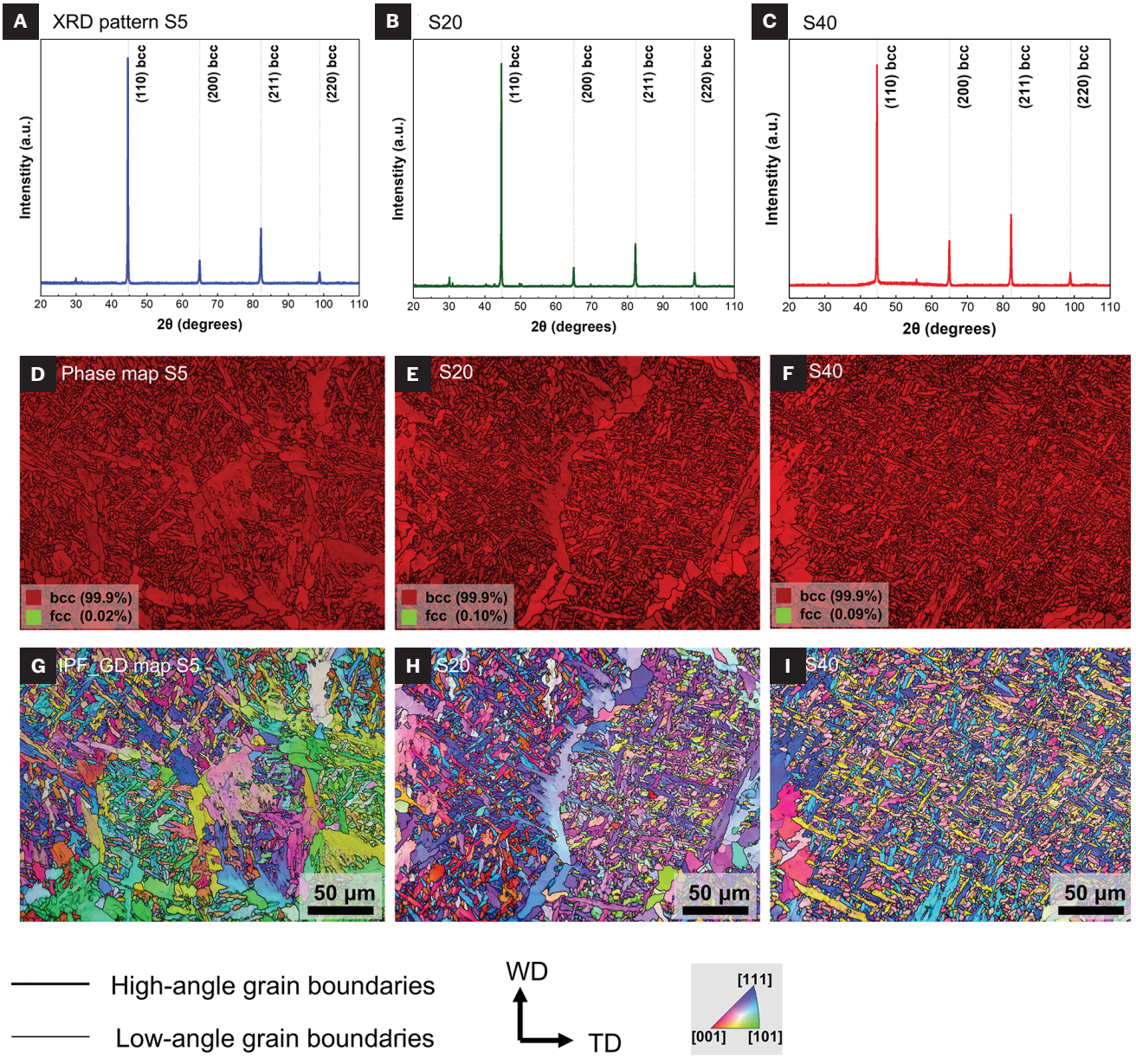

Fig. A-1 — XRD patterns of submerged-arc WMs: A — S5; B — S20; C — S40. EBSD Phase and IPF maps from the ND direction of WMs: D, G — S5; E, H — S20; F, I — S40, respectively. ND denotes the normal direction, WD denotes the welding direction, and TD denotes the transverse direction.

Table A-1 — Quantifications of the Microstructure and Inclusions in S40H Sample

Weld Sample	CG Size (μm)	Volume Fraction			Total Inclusion Number Density (mm^{-2})	Number Density of Inclusions Larger than 1 μm (mm^{-2})
		AF	FSP	GBF		
S40H	84 ± 8	0.278	0.367	0.355	7825	726

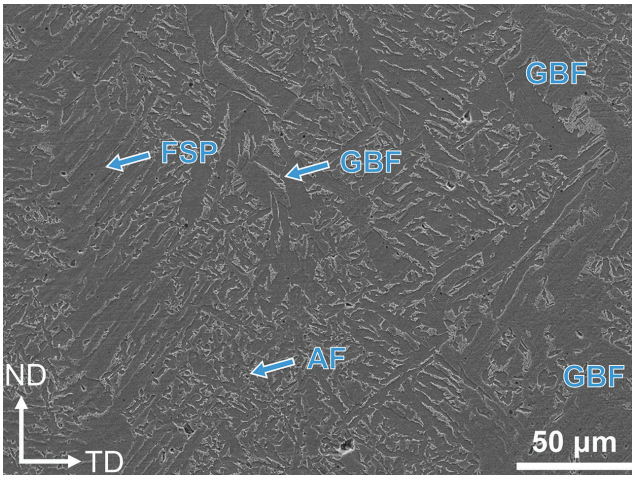

Fig. A-2 — SEM micrograph of S40H sample.

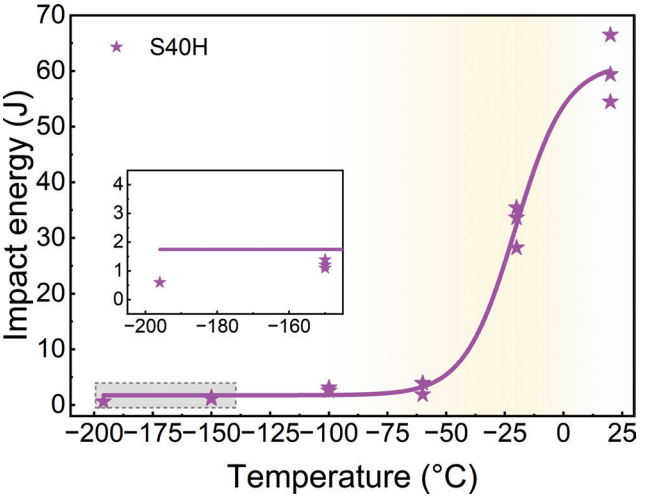

Fig. A-3 — Variation in Charpy V-notch impact energy as a function of testing temperature for welds S40H.

Appendix B

The decomposition of SiO_2 in the flux occurs at the plasma/slag interface subjected to the welding arc (Refs. 14, 31). Chai and Eagar (Ref. 31) argued that SiO_2 in flux was susceptible to decomposition and produced oxygen in the presence of the welding arc plasma, and Reaction A-1 (below) might occur, which will improve the O level of the droplet by increasing the local, as a function of SiO_2, in the flux cavity (Ref. 14). Meanwhile, the chemical reaction that occurred in the slag/metal interface can be shown as Reaction A-2, of which Gibbs-free energy, $\Delta G_2 < 0$ (Detailed calculation of $\Delta G_2 < 0$ for Reaction A-2 is provided elsewhere.) (Ref. 23). Therefore, increased SiO_2 promotes Reactions A-1 and A-2 to the right side, which induces a higher extent of SiO_2 decomposition and increases O and Si levels of the weld pool and is reflected by the increasing amount of O and Si transferred from the slag to the WM. After the droplet is diluted in the weld pool, C is oxidized mainly through Reactions A-3 and A-4 under plasma at the plasma-metal interface according to thermodynamic calculations (Ref. 39). Meanwhile, Mn is lost through Reaction A-5 under the activation of FeO formation, as there is no MnO contained in the slag initially (Ref. 40). Therefore, the rise of SiO_2 level in the flux promotes Reactions A-3 through A-5 to the right side, inducing decarburization and Mn losses from the WMs (Refs. 39, 40).

$$2(SiO_2) \xrightarrow{arc\ plasma} 2SiO(g) + O_2(g) \quad \text{(A-1)}$$

$$(SiO_2) = [Si] + 2[O] \quad \text{(A-2)}$$

$$[C] + [O] = CO(g) \quad \text{(A-3)}$$

$$2[C] + O_2(g) = 2CO(g) \quad \text{(A-4)}$$

$$[Mn] + [O] = (MnO) \quad \text{(A-5)}$$

These element transfer behaviors, as aligned with changes in element contents in Table 2, drive the transition of the non-equilibrium solidification sequence from peritectic to primary δ solidification.

CHAO HAN, **MING ZHONG**, **HANJING ZHU**, **PENG ZUO**, and **CONG WANG** (*wangc@smm.neu.edu.cn*) are with the Key Laboratory for Ecological Metallurgy of Multimetallic Mineral (Ministry of Education), School of Metallurgy, Northeastern University, Shenyang, China.